PCCP

PAPER

View Article Online
View Journal | View Issue

Cite this: *Phys. Chem. Chem. Phys.*, 2023, **25**, 17197

Received 27th February 2023,
Accepted 1st June 2023

DOI: 10.1039/d3cp00907f

rsc.li/pccp

Oxidation and phase transfer of individual Cr-doped dendritic FeO_x particles visualized by full-field nano-XAFS spectroimaging†

Nozomu Ishiguro, *[abc] Hirosuke Matsui,[c] Kohei Wakamatsu,[c] Yoya Suzuki,[c] Oki Sekizawa,[d] Kiyofumi Nitta,[d] Yasuko Terada,[d] Tomoya Uruga[d] and Mizuki Tada*[ac]

Iron oxides with various compositions and polymorphs have been widely used as compounds that require reversible redox properties, such as catalysts. However, partial decomposition during phase transitions often causes irreversible degradation of the redox properties of iron oxides. Cr doping into the crystalline framework of iron oxide dendrites improves the stability of the structural transformation of iron oxides. We spatially visualized the FeO_x-dendrite phase distribution during oxidation in crystalline dendritic FeO_x and Cr-FeO_x particles by full-field nano-X-ray absorption fine structure spectroimaging. The spectroimaging visualized propagation in the phase transitions in the individual FeO_x particles and changes in the phase transition behaviors of the Cr-FeO_x particles. The statistical analysis of the spectroimaging data revealed the phase transition trends in parts of the FeO_x and Cr-FeO_x particles in three Fe density zones (particle thicknesses) and the probability densities of the phase proportions in the dendrites.

1 Introduction

The redox behaviors of solid oxides with oxygen storage and release properties enable these materials to be widely used as cocatalysts in various catalytic systems, such as three-way automobile exhaustion and oxidation. Iron oxides with various stoichiometric compositions and polymorphs show unique chemical and physical properties derived from their crystalline structures. γ-Fe_2O_3 (maghemite) and Fe_3O_4 (magnetite) have similar spinel crystalline structures with octahedral Fe sites (Fe^{2+} and Fe^{3+}) and tetrahedral Fe sites (Fe^{3+}). The topotactic transformation between Fe_3O_4 and γ-Fe_2O_3 provides catalytic functions,[1] but the low thermal stability of the active γ-Fe_2O_3 phase results in a phase transition to the corundum α-Fe_2O_3 phase with an octahedral Fe site.[2]

Many iron oxide particle morphologies have been reported, including nanorods,[1,3] nanocubes,[4] nanoflowers,[5] and dendrites.[6] Doping with transition metals, such as Cr,[7–9] Co,[7,10,11] Ce,[7–10] and Ni,[7,10,12] increases the thermal stability of the spinel FeO_x phases; in particular, Cr-doped iron oxides have been extensively investigated for catalysis.[13–16] We have prepared dendritic FeO_x and Cr-doped FeO_x (Cr-FeO_x) and characterized the local structures and structural transformations of the Cr-FeO_x dendrites by *in situ* Fe K-edge X-ray absorption fine structure (XAFS) and X-ray diffraction.[16] The Cr doping compressed the lattice strain in the iron oxide spinel structures and extended the redox reaction window of spinel γ-Fe_2O_3 by suppressing the structural transformation to α-Fe_2O_3.[16] However, the real-space distribution and propagation of the iron oxide phases in individual crystal particles with the same morphological features of redox structural transformation as for iron dendrites are still unclear.

Combination of X-ray imaging techniques, such as scanning transmission/fluorescence X-ray microscopy (STXM/SFXM),[17–23] full-field transmission X-ray microscopy (FF-TXM),[24–34] coherent X-ray diffraction imaging (CXDI) including X-ray ptychography,[35–42] with X-ray absorption spectroscopy, has been employed to visualize the chemical state distribution in materials.[43] STXM/SFXM or scanning nano-XAFS uses X-ray beams focused by a Fresnel zone plate (FZP) or Kirkpatrick–Baez mirrors on the submicro to

---

[a] Element Visualization Team, Materials Visualization Photon Science Group, RIKEN SPring-8 Center, 1-1-1 Kouto, Sayo, Hyogo 679-5148, Japan
[b] International Center for Synchrotron Radiation Innovation Smart (SRIS)/Institute of Multidisciplinary Research for Advanced Materials (IMRAM), Tohoku University, Katahira 2-1-1, Aoba-ku, Sendai 980-8577, Japan. E-mail: nozomu.ishiguro.c1@tohoku.ac.jp; Tel: +81-22-217-5177
[c] Department of Chemistry, Graduate School of Science/Research Center for Materials Science (RCMS)/Integrated Research Consortium on Chemical Sciences (IRCCS)/Institute for Advanced Study, Nagoya University, Furuchi, Chikusa-ku, Nagoya, Aichi 464-8602, Japan. E-mail: tada.mizuki.u6@f.mail.nagoya-u.ac.jp; Tel: +81-52-788-6200
[d] Japan Synchrotron Radiation Research Institute, SPring-8, 1-1-1 Kouto, Sayo, Hyogo 679-5198, Japan

† Electronic supplementary information (ESI) available: Analysis schemes, Fe K-edge XANES of Fe standard compounds, full-field absorption image, and integrated Fe K-edge XAFS. See DOI: https://doi.org/10.1039/d3cp00907f

nanoscale to obtain X-ray transmission/fluorescence and chemical state images of materials. The resolution is restricted by the specifications of the optical elements, and there is a trade-off between the field-of-view size and the total measurement time.[17–20] Coherent X-ray diffraction imaging techniques, such as X-ray ptychography, have also been developed, in which computational image reconstruction replaces the optical lens to achieve high spatial resolution.[35–42] FF-TXM techniques, such as projection XAFS imaging, achieve full-field chemical state visualization by irradiating the sample with a large X-ray beam and detecting the transmitted X-rays with an X-ray camera. Real-space images with a wide field-of-view can be visualized directly in real space. However, the resolution is limited to X-ray cameras with a micrometer-order pixel size and the technique is used for visualizing large device samples.[25]

Here, we report on the visualization of the spatial distribution of FeO_x phases in dendritic FeO_x single-crystal particles by full-field nano-XAFS imaging with 50 nm spatial resolution. The FF-TXM images using an FZP at the Fe K-edge were recorded for the energy of the Fe K-edge XANES region and the two-dimensional (2D) images of the Fe density, Fe oxidation state, and FeO_x phase proportion were obtained for the oxidation of dendritic Cr-FeO_x crystal particles. The spatially resolved Fe K-edge XANES spectra showed the distribution of chemical states and phase proportions in a number of single particles in the samples simultaneously, with a statistical amount of data that enabled us to investigate the reactions in the heterogeneous oxide particles.

2 Experimental

2.1 Sample preparation

Dendritic FeO_x crystal particles were synthesized by the reported hydrothermal reaction of $K_4[Fe(CN)_6]$,[6,16] and dendritic Cr-FeO_x particles containing 10 mol% (Cr/(Cr+Fe)) Cr were also synthesized by a similar hydrothermal reaction from $K_2Cr_2O_7$ and $K_3[Fe(CN)_6]$, as reported in our previous paper.[16] The as-prepared dendritic FeO_x or 10 wt% Cr-FeO_x was dispersed in ethanol (Wako Chemicals) by sonication. The dispersion was dropped onto a SiN membrane (NTT-AT; 3 × 3 mm, 100 nm thick) with an Au grid printed by lithography (thickness 200 nm), and then the sample was dried in air (Fig. 1B). The Au grid was used as the marker of the correction of the chromatic aberration of the XAFS absorption images. The SiN membranes with the FeO_x crystal particles were observed with an optical microscope to replicate the desired view sight in the full-field XAFS imaging measurements. The as-reduced FeO_x and 10 wt% Cr-FeO_x samples were first reduced under a H_2 flow (99.99%) of 100 mL min^{-1}, heated from 293 to 483 K at 3 K min^{-1}, and then cooled under a He flow (99.999%). The as-reduced FeO_x and Cr-FeO_x crystal

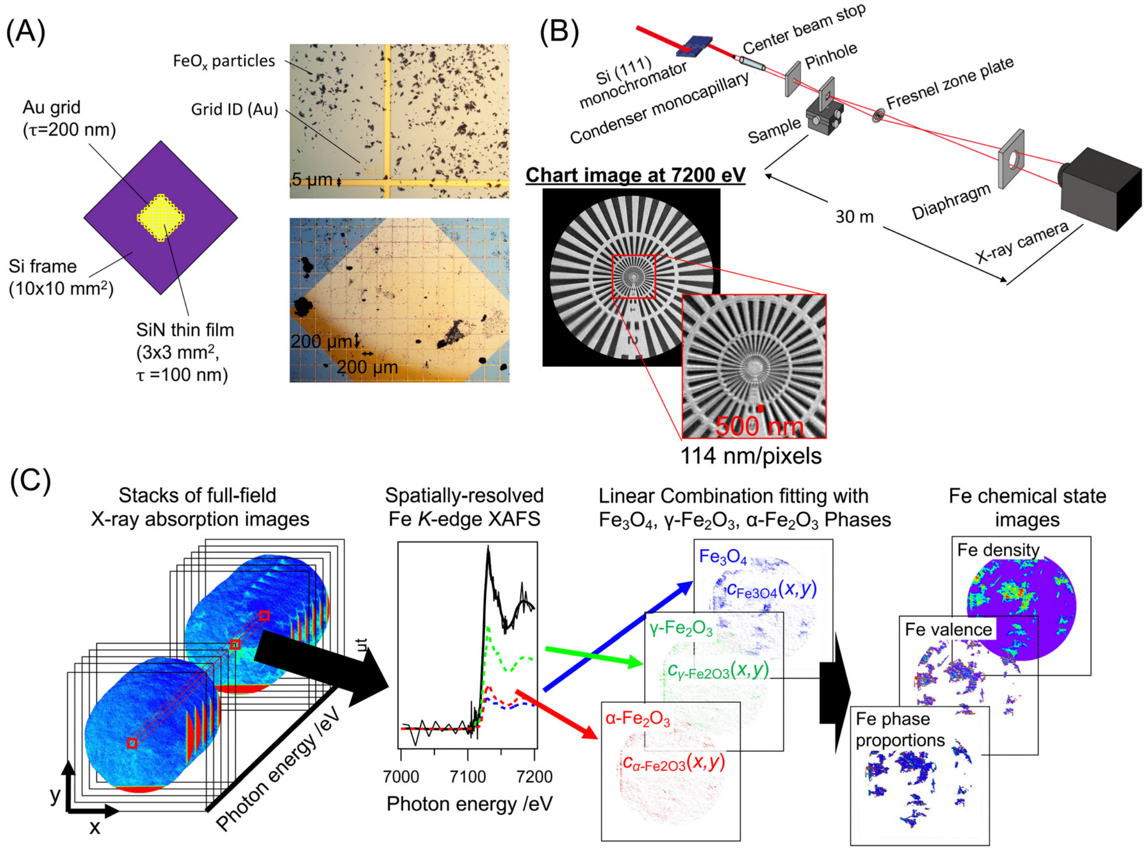

Fig. 1 Schematic of full-field transmission nano-XAFS experiments. (A) Optical setup, (B) membrane sample with FeO_x particles, and (C) analysis schemes from full-field transmission nano-XAFS measurement data to the Fe chemical state images of FeO_x particles.

particles on the SiN membranes were oxidized from room temperature to 423, 473, 523, 573, 603, 623, 653, or 673 K at 3 K min^{-1} under an O_2 flow (99.9%) of 100 mL min^{-1}. After the sample reached the target temperature, the reaction was quenched to room temperature under a He flow.

2.2 Full-field nano-XAFS imaging measurements

Full-field nano-XAFS imaging measurements were carried out at the BL32B2 or BL37XU beamlines at SPring-8 (Hyogo, Japan; 8.0 GeV, 100 mA) (Fig. 1A). X-rays emitted from either bending magnets (BL32B2) or an in-vacuum undulator (BL37XU) were monochromatized by a Si(111) double-crystal monochromator. Higher harmonics were rejected by two vertical mirrors (BL32B2) or horizontal mirrors (BL37XU) placed at the downstream monochromator at an angle of 4 mrad. The monochromatized X-rays were first focused to approximately 100 μm at the focal point by using two pinholes, a center beam stop, and a quartz glass monocapillary. The sample was placed at the focal point and the transmitted X-rays passed through a FZP (Applied Nanotools Inc.; 300 μm diameter, 50 nm outer ring width, 1 μm-thick Au zone). The X-rays diffracted by the FZP formed the image downstream at the X-ray CMOS camera (ORCA-flash 4.0v3, Hamamatsu Photonics) equipped with a gadolinium aluminium gallium garnet (GAGG) scintillator and optical lens, or a SOPHIAS direct-detection X-ray SOI-CMOS camera.[44] The distances from the sample to the FZP (a) and that from the FZP to camera (b) were related to the focal length of the FZP (f) by the lens equation,

$$\frac{1}{a}+\frac{1}{b}=\frac{1}{f} \tag{1}$$

The distance from the sample to the camera, $(a + b)$, was constant (2 m for the BL32B2 system and 23 m for the BL37XU system), whereas the focal length of the FZP (f = 85.9 mm @7.1 keV) depended on the X-ray energy. Therefore, the position of the FZP (XYZ) was synchronously adjusted at every energy point with the monochromator by using feedback stages according to the calibration line initially determined by using an X-ray chart (XRESO-50HC, NTT-AT). Full-field nano-XAFS imaging at the Fe K-edge was performed at 150 energy points at 7.0–7.2 keV At each X-ray energy (E), the $I_0(x,y,E)$ image with the sample offline and the $I_1(x,y,E)$ image with the sample online were recorded with an exposure time of 10 s (Details are given in Table S1, ESI†). To prevent the deterioration of absorption image quality due to instability of the illumination system and the drift of FZP, I_t and I_0 images for each X-ray energy were taken at adjacent time intervals. Using the dark image, $I_{\text{dark}}(x,y)$, recorded without X-ray irradiation, the $I_0(x,y,E)$ and $I_1(x,y,E)$ images were converted to the absorption images, $\mu t(x,y,E)$, by

$$\mu t(\boldsymbol{x},\boldsymbol{y},E)=\ln\left(\frac{I_0(x,y,E)-I_{\text{dark}}(x,y)}{I_1(x,y,E)-I_{\text{dark}}(x,y)}\right) \tag{2}$$

The X-ray absorption of the thin SiN membrane was found to be negligible. To correct the sample drift and magnification rate changes caused by chromatic aberration of the FZP, the $\mu t(x,y,E)$ image stacks were processed using laboratory-made image registration software.[25] Although the contrast of the X-ray absorption of the FeO_x and Cr-FeO_x particles was changed dynamically by the energy at the Fe K-edge, the absorption of the Au grid on the SiN membranes was almost constant and was used as a reference for the image registration processing. The spatial resolution (pixel resolution) of the $\mu t(x,y,E)$ images was estimated to be 114 nm/pixel at 7.1 keV in the BL37XU system.

2.3 Analysis of full-field nano-XAFS spectra

Each pixel in the corrected $\mu t(x,y,E)$ image stacks represents the spatially resolved Fe K-edge XAFS (XANES) spectra. Fe K-edge XANES spectra of dendritic FeO_x and Cr-FeO_x crystal particles were curve-fitted with a linear combination of background line and reference XANES spectra of the Fe_3O_4, γ-Fe_2O_3, and α-Fe_2O_3 phases (Fig. S1, ESI†). The validity of the linear combination curve-fitting analysis for the three components was investigated using the principal component analysis (PCA) and the multivariate curve resolution alternating least squares (MCR-ALS), as described in Fig. S2,ESI.† From each $\mu t(x,y,E)$ pixel, the coefficients $c_{\text{Fe}_3\text{O}_4}(x,y)$, $c_{\gamma\text{-Fe}_2\text{O}_3}(x,y)$, and $c_{\alpha\text{-Fe}_2\text{O}_3}(x,y)$ of Fe_3O_4, γ-Fe_2O_3, and α-Fe_2O_3 were estimated and the 2D plots of the coefficients show the 2D maps of the three FeO_x phases in the sample (Fig. 1C). Parameters for the Fe chemical states, Fe density $\rho(x,y)$, Fe valence $\nu(x,y)$, and proportions of the Fe_3O_4, γ-Fe_2O_3, and α-Fe_2O_3 phases, $\eta_{\text{Fe}_3\text{O}_4}(x,y)$, $\eta_{\gamma\text{-Fe}_2\text{O}_3}(x,y)$, and $\eta_{\alpha\text{-Fe}_2\text{O}_3}(x,y)$, respectively, were converted from the obtained $c_{\text{Fe}_3\text{O}_4}(x,y)$, $c_{\gamma}\text{-Fe}_{2}\text{O}_{3}(x,y)$, and $c_{\alpha}\text{-Fe}_{2}\text{O}_{3}(x,y)$ values (details are provided in Scheme S1, ESI†).

2.4 Probability density analysis of Fe phase proportion in dendritic FeO_x and Cr–FeO_x crystal particles

To investigate the Fe phase proportions in FeO_x and Cr–FeO_x particles, probability densities were estimated from full-field nano-XAFS imaging data by using the kernel density estimation technique. Linear curve fitting analysis result, $\boldsymbol{\mu}_i = (c_{\text{Fe}_3\text{O}_4,i}\ c_{\gamma\text{-Fe}_2\text{O}_3,i}, c_{\alpha\text{-Fe}_2\text{O}_3,i}) = (\eta_{\text{Fe}_3\text{O}_4,i}, \eta_{\gamma\text{-Fe}_2\text{O}_3,i}, \eta_{\alpha\text{-Fe}_2\text{O}_3,i})\rho_i = \boldsymbol{\eta}_i\rho_i$ for every pixel in the nano-XAFS imaging data was used as an independent and uniformly distributed sample. Kernel $p_i(\mu)$, expressing the probability density of μ for i-th sample when μ_i is observed, is calculated using a Gaussian distribution as

$$p_i(\boldsymbol{\mu})=\boldsymbol{\mathcal{N}}(\boldsymbol{\mu}_i,\boldsymbol{\Sigma}_i)=\frac{1}{(2\pi)^{\frac{3}{2}}\sqrt{|\boldsymbol{\Sigma}_i|}}\exp\left\{-\frac{1}{2}{}^{t}_{\circ}(\boldsymbol{\mu}-\boldsymbol{\mu}_i)\Sigma_i^{-1}(\boldsymbol{\mu}-\boldsymbol{\mu}_i)\right\} \tag{3}$$

whereas $\boldsymbol{\Sigma}_i^{-1}$ is obtained from the linear curve fitting covariation matrix. Kernel density $P(\boldsymbol{\mu})$ is estimated as

$$P(\boldsymbol{\mu})=\frac{1}{N}\sum_{i=0}^{N-1}p_i(\boldsymbol{\mu})=\frac{1}{N}\sum_{i=0}^{N-1}p_i(\boldsymbol{\eta}\rho)=P(\boldsymbol{\eta},\rho) \tag{4}$$

where $P(\boldsymbol{\mu})$ can also be interpreted as a function of $\boldsymbol{\eta}$ and ρ, $P(\boldsymbol{\eta}|\rho)$. Finally, probability density $P(\boldsymbol{\eta})$ of Fe phase proportion $\boldsymbol{\eta}$ is given by

$$P(\boldsymbol{\eta})=\frac{1}{N}\int_0^{\infty}P(\boldsymbol{\eta},\rho)\rho^2\mathrm{d}\rho \tag{5}$$

The details of the analyses are summarized in Scheme S1 (ESI†).

3 Results and discussion

3.1 Visualization of Fe chemical states and phase changes in dendritic FeO_x and Cr–FeO_x particles during oxidation

The as-prepared dendritic FeO_x and Cr–FeO_x particles consisting of the α-Fe_2O_3 phase[16] were reduced with H_2 at temperatures from room temperature to 483 K to obtain the as-reduced samples. Fig. S3A–C (ESI†) show full-field X-ray absorption images at 7.130 keV of dendritic FeO_x and Cr–FeO_x on a SiN membrane with Au grids and Fe K-edge XANES spectra of all FeO_x or Cr–FeO_x particles in the full-field image. The linear combination curve-fitting analysis of the Fe K-edge XANES spectra showed that as-reduced FeO_x and Cr–FeO_x consisted of the Fe_3O_4 phase (Fig. S3B1 and D1, ESI†). The Fe K-edge XANES spectra of FeO_x after oxidation at 473 and 573 K showed that the main phase was γ-Fe_2O_3, although unreacted Fe_3O_4 and overreacted α-Fe_2O_3 phases were present (Fig. S3B2 and B3, ESI†). After oxidation at 623 K, the Fe_3O_4 phase was consumed and the α-Fe_2O_3 phase was formed in the FeO_x sample without Cr (Fig. S3B4, ESI†).

In contrast, Cr–FeO_x particles containing 10 wt% Cr showed different oxidation behaviors and the γ-Fe_2O_3 phase was selectively formed after oxidation at 473 and 573 K. The γ-Fe_2O_3 phase remained even after oxidation at 673 K and the formation of the α-Fe_2O_3 phase was negligible (Fig. S3D2–D4, ESI†). The oxidation temperature profiles of the Fe valence and the FeO_x phase proportions (Fig. 2) showed that the Cr–FeO_x particles were oxidized from Fe_3O_4 to γ-Fe_2O_3 at a slightly lower temperature than the FeO_x particles without Cr, indicating that the stability of the γ-Fe_2O_3 phase was higher than in the FeO_x particles.

Fig. 3 and 4 show the full-field XAFS images of the dendritic FeO_x and Cr–FeO_x particles, revealing the structures and reaction trends in the particles. We obtained optical microscopy images (A) and plotted the Fe density images (B), Fe valence images (C), and Fe phase proportion images of the FeO_x and Cr–FeO_x particles before and after oxidation at different temperatures from linear combination curve fitting of the spatially resolved Fe K-edge XAFS at a resolution of approximately 100 nm. The Fe density images were consistent with the optical microscopy images, suggesting that the full-field X-ray imaging captured the structures of the dendritic particles. The FeO_x and Cr–FeO_x particles both showed contrasts in the Fe density image, in which the leaf-vein-like stem of the particles had a high Fe density surrounded by lower Fe density regions (Fig. 3B and C).

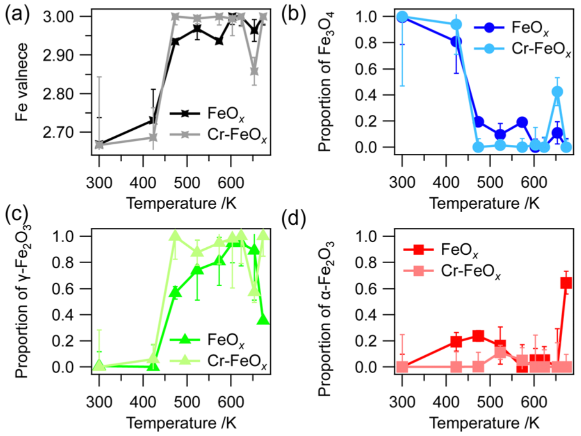

Fig. 2 Oxidation temperature profiles of (a) Fe valence and Fe phase proportions of (b) Fe_3O_4, (c) γ-Fe_2O_3, and (d) α-Fe_2O_3, obtained from the integration of full-field XAFS spectra in the particle regions for dendritic FeO_x and dendritic 10 wt% Cr–FeO_x in Fig. S3 (ESI†).

The 2D mapping images indicated a non-uniform distribution of the Fe valence and Fe phase proportion in the dendritic particles, although their averages followed the trends observed in the Fe K-edge XAFS spectra. A large area of the Fe valence map of the as-reduced FeO_x particles was $Fe^{2.67+}$ (purple) and the phase proportion map showed the Fe_3O_4 phase (blue), whereas there were oxidized spots of the α-Fe_2O_3 and γ-Fe_2O_3 phases, shown as Fe^{3+} (red) (Fig. 3C1 and D1). After oxidation at 473 K, there was an increase in the oxidized regions, and the oxidation was almost complete at 573 K, where Fe^{3+} (red) was the main valence state (Fig. 3C2 and C3). Accompanying the changes in the Fe valence state in the dendritic particles, the phase proportion of the particles also changed from Fe_3O_4 (blue) to γ-Fe_2O_3 (green) (Fig. 3D2 and D3). After the reaction at 673 K, the phase proportion image suggested a phase transition to α-Fe_2O_3 in some parts of the particles (red regions in Fig. 3D4).

For dendritic 10 wt% Cr–FeO_x, the main region in the Fe density map of the as-reduced sample particles was also $Fe^{2.67+}$ (purple) and the blue zone in the phase proportion map was assigned to the Fe_3O_4 phase (Fig. 4C1 and D1), similar to dendritic FeO_x without Cr. After oxidation at 473 K, the majority of the Fe valence image was Fe^{3+} (red) and the phase proportion image suggested the formation of γ-Fe_2O_3 (green) (Fig. 4C2 and D2). Similar trends were observed for the sample oxidized at 573 K (Fig. 4C3 and D3). The phase transition to α-Fe_2O_3 was negligible for 10 wt% Cr–FeO_x oxidized at 673 K (Fig. 4D4), indicating that Cr–FeO_x showed stability against the phase transition to α-Fe_2O_3 compared with FeO_x without Cr. The full-field XAFS images also showed that there were small domains of partially non-uniform Fe valence or Fe phase proportion in the dendritic particles although the majorities of the pixels in the images behaved similarly to the average of the images or the powder assemblies.

3.2 Statistical analysis of FeO_x phase proportion trends for the oxidation of dendritic FeO_x and Cr–FeO_x particles

The full-field XAFS imaging clearly visualized the changes in the FeO_x phases after the oxidation of the dendritic FeO_x and Cr–FeO_x particles and there were differences in the phase proportion between the FeO_x and Cr–FeO_x particles (Fig. 3 and 4). We performed a statistical analysis of the phase proportions of the FeO_x and Cr–FeO_x particles by using the 2D XAFS imaging data (Fig. 5 and 6). First, the probability density $P(\boldsymbol{\eta})$ of the phase proportion coordinates, $\boldsymbol{\eta} = (\eta_{Fe_3O_4}, \eta_{\gamma\text{-}Fe_2O_3}, \eta_{\alpha\text{-}Fe_2O_3})$, of the FeO_x and Cr–FeO_x particles was statistically estimated in all effective pixels in the full-field nano-XAFS imaging data by using the kernel density estimation method. The estimated

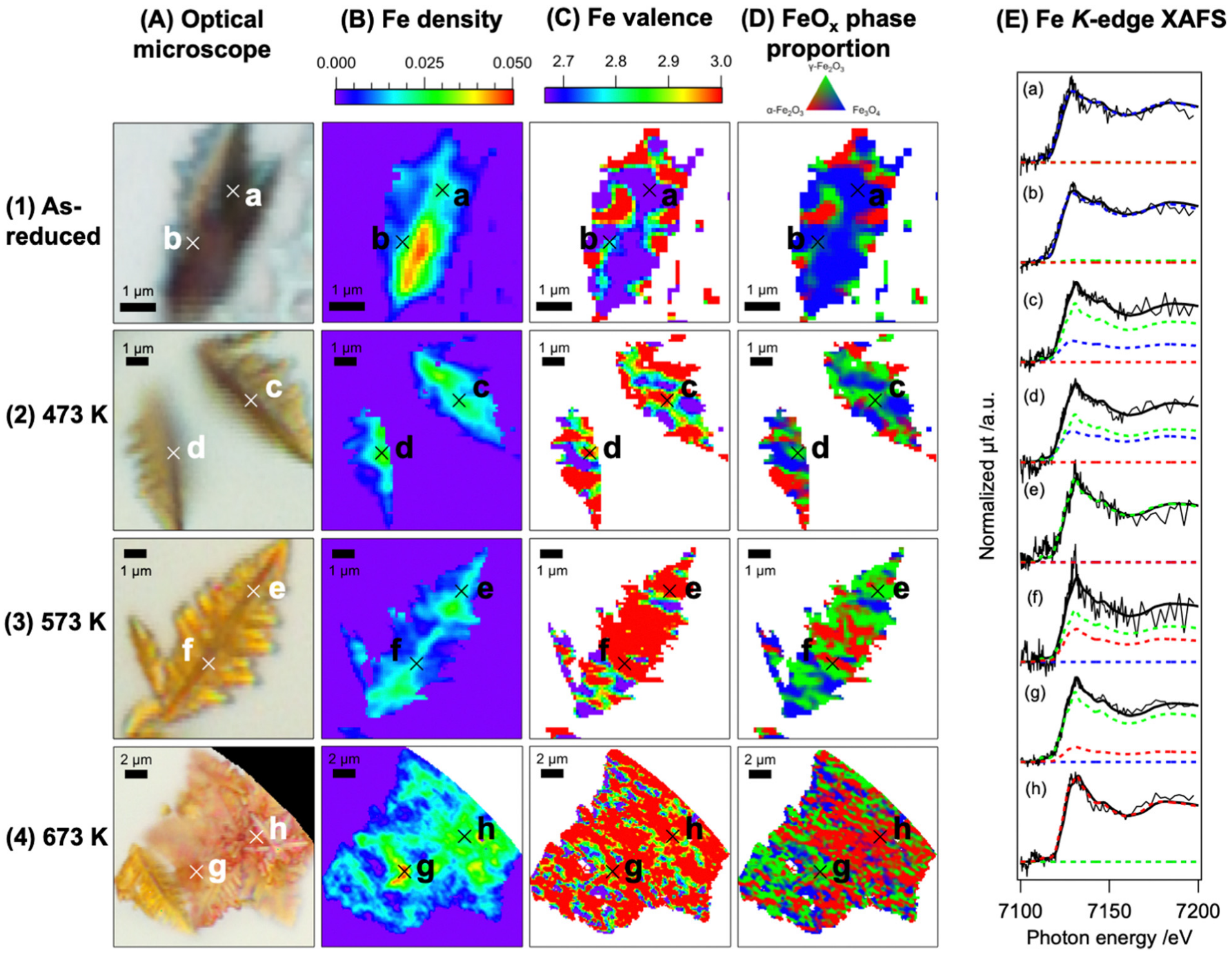

Fig. 3 (A) Optical microscopy images, (B) Fe density images, (C) Fe valence images, and (D) Fe phase proportion images after oxidation of dendritic FeO$_x$ at different temperatures. (1) As-reduced and after oxidation at (2) 423, (3) 573, and (4) 673 K. All the images of (A) were taken after the XAFS measurements. (E) Spatially resolved Fe K-edge XAFS spectra of selected points (×) in A–D. Black solid lines: observed data; black bold lines: linear combination of fitting data; blue dashed bold lines: fraction of the Fe$_3$O$_4$ phase; green dashed bold lines: fraction of the γ-Fe$_2$O$_3$ phase; red dashed bold lines: fraction of the α-Fe$_2$O$_3$ phase.

probability densities for the FeO$_x$ and Cr–FeO$_x$ particles are shown in Fig. 5A and 6A, respectively, in which the probability densities of the phases in the FeO$_x$ and Cr–FeO$_x$ particles are plotted on ternary diagrams. If $P(\boldsymbol{\eta})$ is higher in the right, top, or left corners of the ternary diagram, the Fe$_3$O$_4$, γ-Fe$_2$O$_3$, and α-Fe$_2$O$_3$ phases, respectively, tend to be distributed stochastically in the particle. If $P(\boldsymbol{\eta}_{\max})$ is large and the density distribution is dense, the non-uniformity is small.

Table S2 (ESI†) shows the maximum probability densities in the ternary diagrams in Fig. 5 and 6. For the as-reduced FeO$_x$ particles, the probability density reached a maximum ($P(\boldsymbol{\eta}_{\max})$ = 7.462) at $\boldsymbol{\eta}_{\max}$ = (96%, 0%, and 4%), in the right corner of the ternary diagram (Fig. 5A1). After oxidation at 473 K, the phase density median moved to the top corner (γ-Fe$_2$O$_3$), where $P(\boldsymbol{\eta}_{\max})$ = 2.423 at $\boldsymbol{\eta}_{\max}$ = (21%, 68%, and 11%), and the density spread in the (Fe$_3$O$_4$–γ-Fe$_2$O$_3$) direction (Fig. 5A2). This broad distribution indicated that the oxidation from Fe$_3$O$_4$ to γ-Fe$_2$O$_3$ was incomplete. After oxidation at 573 K, where the maximum probability density was almost steady ($P(\boldsymbol{\eta}_{\max})$ = 4.011 at $\boldsymbol{\eta}_{\max}$ = (6%, 89%, and 5%)), the probability density spread in the (γ-Fe$_2$O$_3$–α-Fe$_2$O$_3$) direction. This change in direction indicated that the oxidation from Fe$_3$O$_4$ to γ-Fe$_2$O$_3$ was almost complete, and the phase transformation from γ-Fe$_2$O$_3$ to α-Fe$_2$O$_3$ had started (Fig. 5A3). Finally, after oxidation at 673 K, the maximum density moved to near the left corner (α-Fe$_2$O$_3$ side), where $P(\boldsymbol{\eta}_{\max})$ = 2.423 at $\boldsymbol{\eta}_{\max}$ = (7%, 28%, and 65%), and the probability density still spread in the (γ-Fe$_2$O$_3$–α-Fe$_2$O$_3$) direction (Fig. 5A4).

For the Cr–FeO$_x$ particles, the maximum point for the as-reduced conditions was also in the right corner (Fe$_3$O$_4$), where $P(\boldsymbol{\eta}_{\max})$ = 5.031 at $\boldsymbol{\eta}_{\max}$ = (95%, 5%, and 0%) (Fig. 6A1). The Cr–FeO$_x$ particles also started to oxidize at 473 K ($P(\boldsymbol{\eta}_{\max})$ = 2.883 at $\boldsymbol{\eta}_{\max}$ = (14%, 81%, and 5%)) (Fig. 6A2), and oxidation was complete at 573 K ($P(\boldsymbol{\eta}_{\max})$ = 3.519 at $\boldsymbol{\eta}_{\max}$ = (9%, 85%, and 6%)) (Fig. 5A3). Fig. 6A2 and A3 show the probability density spreading in the (Fe$_3$O$_4$–γ-Fe$_2$O$_3$) and (γ-Fe$_2$O$_3$–α-Fe$_2$O$_3$) directions, respectively, similar to the FeO$_x$ particles, indicating smooth oxidation to γ-Fe$_2$O$_3$ and a slow phase transformation to

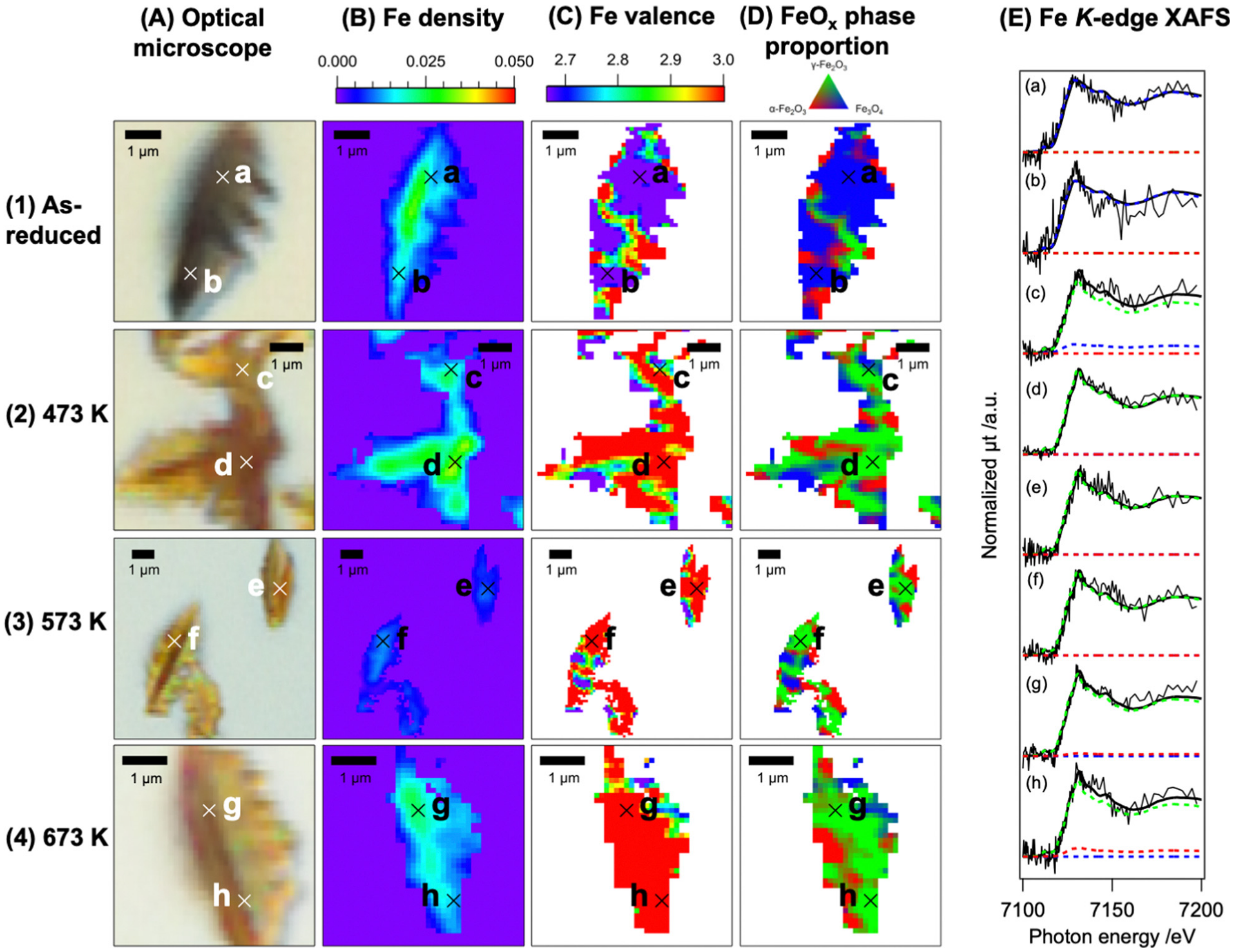

Fig. 4 (A) Optical microscopy images, (B) Fe density images, (C) Fe valence images, and (D) Fe phase proportion images after oxidation of dendritic 10 wt% Cr–FeO$_x$ at different temperatures. (1) As-reduced and after oxidation at (2) 423, (3) 573, and (4) 673 K. All the images of (A) were taken after the XAFS measurements. (E) Spatially resolved Fe K-edge XAFS spectra of selected points (×) in A–D. Black solid lines: observed data; black bold lines: linear combination fitting data; blue dashed bold lines: fraction of the Fe_3O_4 phase; green dashed bold lines: fraction of the γ-Fe_2O_3 phase; red dashed bold lines: fraction of the α-Fe_2O_3 phase.

α-Fe_2O_3. The greatest difference between the FeO$_x$ and Cr–FeO$_x$ particles was observed at 673 K, where the maximum probability density point was near γ-Fe_2O_3 ($P(\boldsymbol{\eta}_{\max}) = 4.332$ at $\boldsymbol{\eta}_{\max}$ = (4%, 88%, and 8%)) and the phase transformation to α-Fe_2O_3 had not started in the Cr–FeO$_x$ particles (Fig. 6A4).

We prepared Fe density histograms of the particles (Fig. 5B and 6B) and classified the histograms into Fe density zones of (i) thin, (ii) medium, and (iii) thick. The posterior probability density of the FeO$_x$ phase proportions with pixels belonging to each zone (i)–(iii) was plotted (Fig. 5C and 6C), and the Fe phase proportion belonging to each of zones (i)–(iii) was also imaged (Fig. 5D and 6D). The ternary diagrams of the posterior probability density for zones (i)–(iii) showed distinctive trends in probability density for the phase proportion in the FeO$_x$ and Cr–FeO$_x$ particles.

The posterior probability densities in zone (i), corresponding to regions that had lower Fe density, showed smaller differences in probability density for both FeO$_x$ and Cr–FeO$_x$. The maximum densities were nearer to the left corner (α-Fe_2O_3) than in the full-field ternary diagram (Fig. 5Ci and 6Ci), regardless of the reaction conditions. The lower contrast in the probability density ternary diagrams of zone (i) indicated that the proportion of either type of Fe phase was uncertain. These pixels assigned to zone (i) were mainly at the edge sites of the particles (Fig. 5Di and 6Di).

The ternary diagrams of zone (iii) with higher Fe density showed different behaviors from those of zone (i) for oxidation (Fig. 5C-iii). Most of the as-reduced FeO$_x$ and Cr–FeO$_x$ particles consisted of Fe_3O_4 (Fig. 5D1-iii and 6D1-iii). After oxidation at 473 K, the red regions of the ternary diagrams were shifted to γ-Fe_2O_3 from Fe_3O_4 (Fig. 5C2-iii and 6C2-iii), and the shift in Cr–FeO$_x$ was clearer than that in FeO$_x$. Then, after oxidation at 573 K, the ternary diagrams shows that the γ-Fe_2O_3 phase became dominant (Fig. 5D3-iii and 6D3-iii). There were large differences in the phase proportions in the FeO$_x$ and Cr–FeO$_x$ particles in the ternary diagrams after oxidation at 673 K (Fig. 5C4-iii and 6C4-iii). The red region with a high probability density zone (iii) in the Cr–FeO$_x$ particles was localized at the top (γ-Fe_2O_3). In contrast, the corresponding region for the FeO$_x$

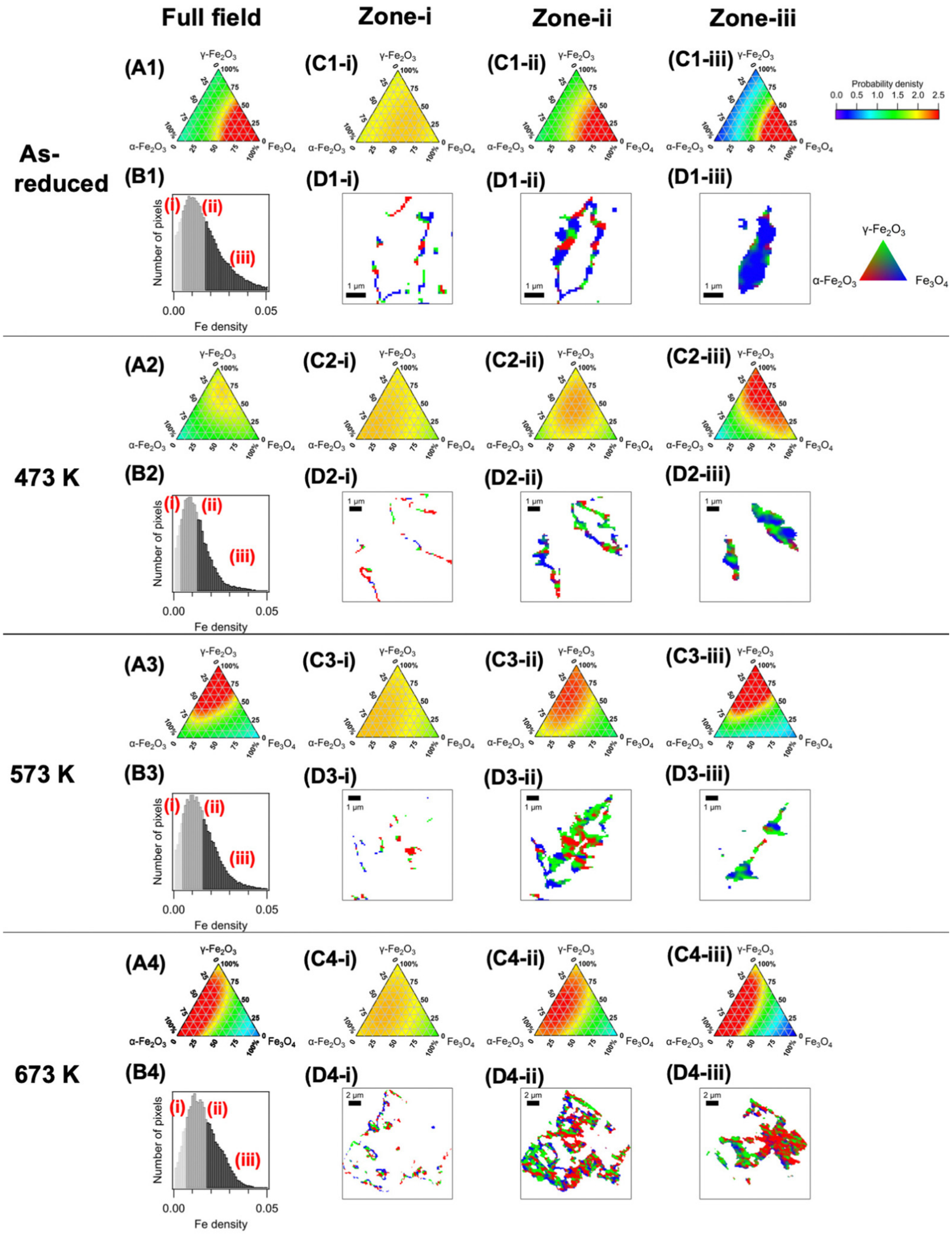

Fig. 5 Probability density analysis of the dendritic FeO_x particles (1) as-reduced and after oxidation at (2) 473, (3) 573, and (4) 673 K. (A) Ternary probability density of the Fe phase proportion, (B) Fe density histograms, (C) ternary posterior probability density diagram, and (D) Fe phase proportion images in specific Fe density ($\Delta\mu t$) range zones (i)–(iii). Zone (ii) was defined as a range of 50%, including the Fe density histogram mode in (B), and zones (i) and (iii) were defined as the ranges before and after that of zone (ii), respectively.

particles was widely distributed between γ-Fe_2O_3 and α-Fe_2O_3, and was not localized at the corners of γ-Fe_2O_3 and α-Fe_2O_3. These results indicate that the FeO_x transition proceeded across the whole of the dendritic particles. Similar trends were observed in zone (ii) with the medium Fe density.

The ternary diagrams of the Fe phase proportion for Fe density zones (i)–(iii) revealed the following trends in the reactivity and phase transition of the dendritic FeO_x and Cr–FeO_x particles during oxidation.

(1) The α-Fe_2O_3 phase tended to be produced in the thinner parts (zone (i)) of dendritic FeO_x and Cr–FeO_x. These parts were mainly located on the outer surface of the dendritic particles, which has low crystallinity compared with the bulk, and these parts showed different behaviors compared with zones (ii) and (iii).

(2) Two modes of oxidation were observed in the probability density diagrams: the $Fe_3O_4 \rightarrow \gamma$-$Fe_2O_3$ transition (from the right corner to the top corner in the diagram) and the

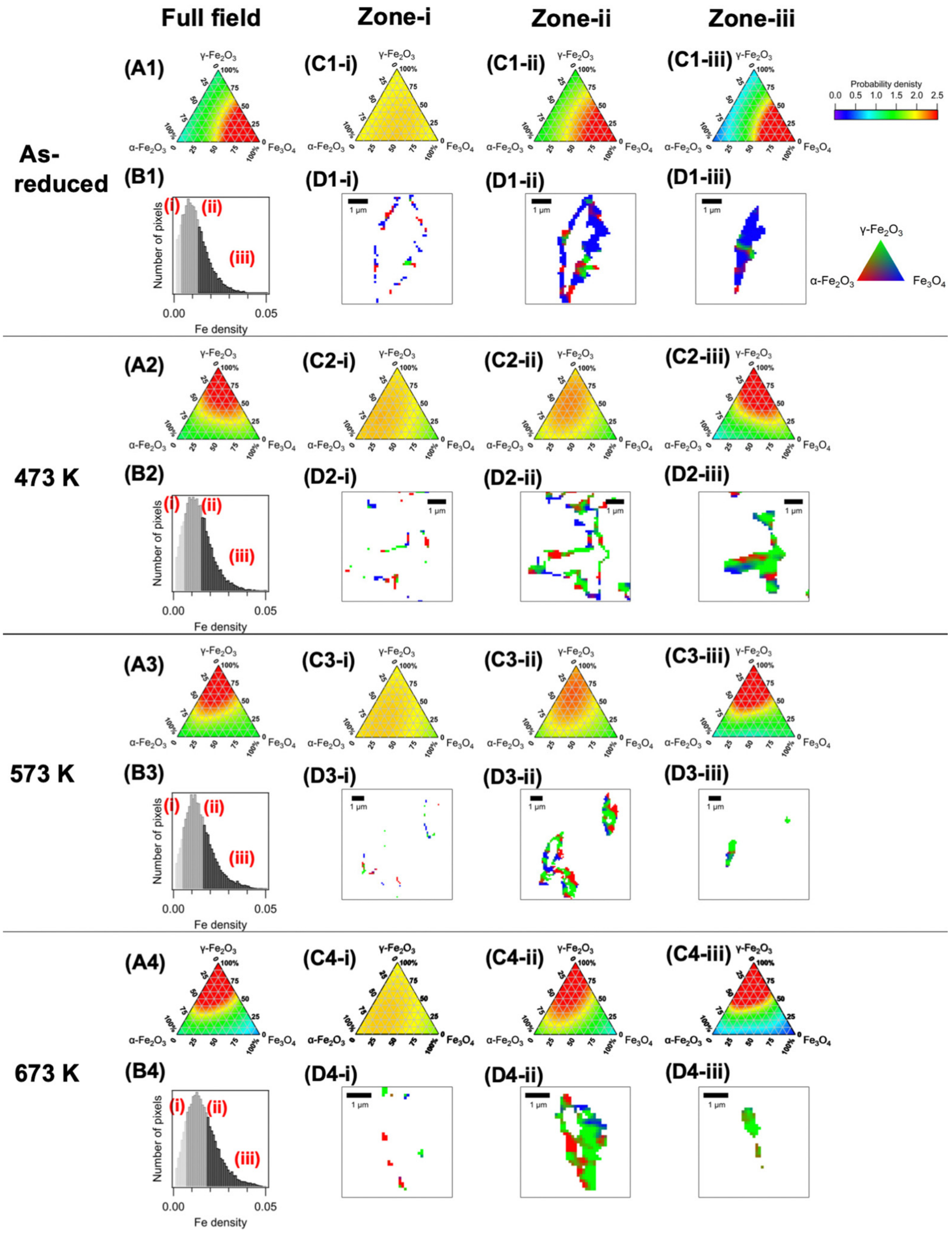

Fig. 6 Probability density analysis of the dendritic 10 wt% Cr–FeO$_x$ particles (1) as-reduced and after oxidation at (2) 473, (3) 573, and (4) 673 K. (A) Ternary probability density of the Fe phase proportion, (B) Fe density histograms, (C) ternary posterior probability density diagram, and (D) Fe phase proportion images in specific Fe density ($\Delta\mu t$) range zones (i)–(iii). Zone (ii) was defined as a range of 50%, including the Fe density histogram mode in (B), and zones (i) and (iii) were defined as the ranges before and after that of zone (ii), respectively.

γ-Fe_2O_3 → α-Fe_2O_3 transition (from the top corner to the left corner). The XAFS analysis of the powder assemblies of the FeO$_x$ and Cr–FeO$_x$ dendrites suggested the negligible formation of α-Fe_2O_3 below 550 K, but spatial imaging by full-field imaging XAFS suggested a fine distribution of the minor phases in each dendritic particle, suggesting that the two oxidation modes coexisted during thermal oxidation. The local phase transition to the α-Fe_2O_3 would structurally interfere with smooth redox propagation between the Fe_3O_4 and γ-Fe_2O_3 phases, which tends to create a non-uniform phase distribution within the particles.

(3) The Cr doping in the Cr–FeO$_x$ particles led to the appearance of a thick body of dendrites and the strong suppression of the second phase transition from γ-Fe_2O_3 to α-Fe_2O_3 was clearly observed in the Cr–FeO$_x$ dendrites.

These results demonstrated that the Cr doping in the Cr–FeO$_x$ dendrites increased the reactivity for the first oxidation of Fe_3O_4 → γ-Fe_2O_3 and improved the stability against the phase transformation to the α-Fe_2O_3 phase in the body of the dendritic particles. Full-field XAFS chemical imaging revealed the heterogeneous distribution of the structure, oxide phases, and reactive pathways of actual oxide particles.

Conclusions

Full-field XAFS imaging visualized the real-space distribution of the Fe oxidation state and phase proportions of the Fe_3O_4, γ-Fe_2O_3, and α-Fe_2O_3 phases in dendritic FeO_x and 10 wt% Cr–FeO_x particles. We also visualized the changes in the Fe oxidation state and phase proportions during the oxidation and phase transitions of the dendrites. The statistical analysis of the Fe phase proportion images revealed different phase proportion modes that depended on the Fe density (thickness) of the crystal particles and on the Cr dopant. The suppression of the phase transition from γ-Fe_2O_3 to α-Fe_2O_3 was greater in the thick body of the Cr–FeO_x particles. These observations suggested that instability in the thin particle region was one cause of the phase transformation to the α-Fe_2O_3 phase, which suppresses the oxygen storage capacity of FeO_x materials and degrades their catalytic performance.

Author contributions

N. I.: conceptualization, data curation, methodology, software, funding acquisition, investigation, visualization, project administration and writing – original draft preparation. H.M.: funding acquisition, investigation, methodology, investigation, and resources. K. W. and J. K.: investigation, and resource. O. S., K. N., Y. T. and T. U.: investigation and methodology. M. T.: conceptualization, funding acquisition, methodology, project administration, supervision, and writing – reviewing and editing.

Conflicts of interest

There are no conflicts to declare.

Acknowledgements

This work was supported by KAKENHI (Grant No. 16K17863 and 167K18288), JSPS KAKENHI Grant-in-Aid for Scientific Research (B) (26288005, 18H01940, and 22H02031), and RIKEN SPring-8. XAFS measurements were performed at SPring-8 (No. 2015A1125, 2015A1559, 2016B1330, 2017B1852, 2018A1332, and 2018B1343). We thank Ms Noriko Takada (Institute for Molecular Science) for Au grid fabrication on the SiN membranes.

Notes and references

1 X. Mou, Y. Li, B. Zhang, L. Yao, X. Wei, D. S. Su and W. Shen, *Eur. J. Inorg. Chem.*, 2012, 2684–2690.

2 J. Lai, K. V. P. M. Shafi, K. Loos, A. Ulman, Y. Lee, T. Vogt and C. Estournès, *J. Am. Chem. Soc.*, 2003, **125**, 11470–11471.

3 X. Mou, B. Zhang, Y. Li, L. Yao, X. Wei, D. S. Su and W. Shen, *Angew. Chem., Int. Ed.*, 2012, **51**, 2989–2993.

4 R. Wang, C. Xu, J. Sun and L. Gao, *Sci. Rep.*, 2014, **4**, 7171.

5 B. Wang, J. Sun, M. Abbas, Y. Liu, F. Kong, H. Xiao and J. Chen, *Catal. Lett.*, 2017, **147**, 1153–1161.

6 V. Polshettiwar, M. N. Nadagouda and R. S. Varma, *Chem. Commun.*, 2008, 6318–6320.

7 A. Khan, P. Chen, P. Boolchand and P. G. Smirniotis, *J. Catal.*, 2008, **253**, 91–104.

8 G. K. Reddy and P. G. Smirniotis, *Ind. Eng. Chem. Res.*, 2017, **56**, 1772–1781.

9 G. K. Reddy, K. Gunasekera, P. Boolchand, J. Dong and P. G. Smirniotis, *J. Phys. Chem. C*, 2011, **115**, 7586–7595.

10 G. K. Reddy, P. Boolchand, J. Dong and P. G. Smirniotis, *J. Phys. Chem. C*, 2012, **116**, 11019–11031.

11 O. Voniuk, C. Bazzo, S. Albonetti, N. Tanchoux, F. Bosselet, J.-M. M. Millet, F. D. Renzo and F. Cavani, *ChemCatChem*, 2017, **9**, 2219–2230.

12 D.-W. Lee, M. S. Lee, J. Y. Lee, S. Kim, H.-J. Eom, D. J. Moon and K.-Y. Lee, *Catal. Today*, 2013, **210**, 2–9.

13 C. J. Keturakis, M. Zhu, E. K. Gibson, M. Daturi, F. Tao, A. I. Frenkel and I. E. Wachs, *ACS Catal.*, 2016, **6**, 4786–4798.

14 M. Zhu, T. C. R. Rocha, T. Lunkenbein, A. Knop-Gericke, R. Schlögl and I. E. Wachs, *ACS Catal.*, 2016, **6**, 4455–4464.

15 M. Zhu and I. E. Wachs, *ACS Catal.*, 2016, **6**, 722–732.

16 H. Matsui, N. Ishiguro, Y. Suzuki, K. Wakamatsu, C. Yamada, K. Sato, N. Maejima, T. Uruga and M. Tada, *Phys. Chem. Chem. Phys.*, 2020, **22**, 28093.

17 M. Tada, N. Ishiguro, T. Uruga, H. Tanida, Y. Terada, S. Nagamatsu, Y. Iwasawa and S. Ohkoshi, *Phys. Chem. Chem. Phys.*, 2011, **13**, 14910–14913.

18 N. Ishiguro, T. Uruga, O. Sekizawa, T. Tsuji, M. Suzuki, N. Kawamura, M. Mizumaki, K. Nitta, T. Yokoyama and M. Tada, *ChemPhysChem*, 2014, **15**, 1563–1568.

19 X. Yu, H. Pan, Y. Zhou, P. Northrup, J. Xiao, S. Bak, M. Liu, K.-W. Nam, D. Qu, J. Liu, T. Wu and X.-Q. Yang, *Adv. Energy Mater.*, 2015, **5**, 1500072.

20 H. Matsui, N. Ishiguro, K. Enomoto, O. Sekizawa, T. Uruga and M. Tada, *Angew. Chem., Int. Ed.*, 2016, **55**, 12022–12025.

21 M.-J. Wang, F.-D. Yu, G. Sun, J. Wang, J.-G. Zhou, D.-M. Gu and Z.-B. Wang, *J. Mater. Chem. A*, 2019, **7**, 8302–8314.

22 W. Li, Z. Wang, F. Zhao, M. Li, X. Gao, Y. Zhao, J. Wang, J. Zhou, Y. Hu, Q. Xiao, X. Cui, M. J. Eslamibidgoli, M. H. Eikerling, R. Li, F. Brandys, R. Divigalpitiya, T.-K. Sham and X. Sun, *Chem. Mater.*, 2020, **32**, 1272–1280.

23 X. Ye, J. E. Schmidt, R. P. Wang, I. K. van Ravenhorst, R. Oord, T. Chen, F. de Groot, F. Meirer and B. M. Weckhuysen, *Angew. Chem., Int. Ed.*, 2020, **59**, 15610–15617.

24 L. Li, Y. C. Chen-Wiegart, J. Wang, P. Gao, Q. Ding, Y. S. Yu, F. Wang, J. Cabana, J. Wang and S. Jin, *Nat. Commun.*, 2015, **6**, 6883.

25 H. Matsui, N. Ishiguro, T. Uruga, O. Sekizawa, K. Higashi, N. Maejima and M. Tada, *Angew. Chem., Int. Ed.*, 2017, **56**, 9371–9375.

26 S. Kuppan, Y. Xu, Y. Liu and G. Chen, *Nat. Commun.*, 2017, **8**, 14309.

27 S. Shulda, J. N. Weker, C. Ngo, S. M. Alia, S. A. Mauger, K. C. Neyerlin, B. S. Pivovar and S. Pylypenko, *ACS Appl. Nano Mater.*, 2018, **2**, 525–534.

28 C. S. Kaira, C. Kantzos, J. J. Williams, V. De Andrade, F. De Carlo and N. Chawla, *Acta Mater.*, 2018, **144**, 419–431.

29 C. Zhao, T. Wada, V. De Andrade, V. Gürsoy, H. Kato and Y.-C. K. Chen-Wiegart, *Nano Energy*, 2018, **52**, 381–390.

30 J. Y. Park, J. P. Singh, J. Lim, K. H. Chae and S. Lee, *Mater. Lett.*, 2020, **261**, 126983.

31 T. Li, C. Lim, Y. Cui, X. Zhou, H. Kang, B. Yan, M. L. Meyerson, J. A. Weeks, Q. Liu, F. Guo, R. Kou, Y. Liu, V. De Andrade, F. De Carlo, Y. Ren, C.-J. Sun, C. B. Mullins, L. Chen, Y. Fu and L. Zhu, *J. Mater. Chem. A*, 2020, **8**, 750–759.

32 S. Spence, W. Lee, F. Lin and X. Xiao, *Nanotechnology*, 2021, **32**, 442003.

33 Y. Kim and J. Lim, *Sci. Rep.*, 2022, **12**, 2894.

34 D. Hou, Z. Xu, Z. Yang, C. Kuai, Z. Du, C.-J. Sun, Y. Ren, J. Liu, X. Xiao and F. Lin, *Nat. Commun.*, 2022, **13**, 3437.

35 D. A. Shapiro, Y. S. Yu, T. Tyliszczak, J. Cabana, R. Celestre, W. Chao, K. Kaznatcheev, A. L. Kilcoyne, F. Maia, S. Marchesini, Y. S. Meng, T. Warwick, L. L. Yang and H. A. Padmore, *Nat. Photonics*, 2014, **8**, 765–769.

36 Y. S. Yu, M. Farmand, C. Kim, Y. Liu, C. P. Grey, F. C. Strobridge, T. Tyliszczak, R. Celestre, P. Denes, J. Joseph, H. Krishnan, F. R. Maia, A. L. Kilcoyne, S. Marchesini, T. P. C. Leite, T. Warwick, H. Padmore, J. Cabana and D. A. Shapiro, *Nat. Commun.*, 2018, **9**, 1–7.

37 M. Farmand, R. Celestre, P. Denes, A. L. D. Kilcoyne, S. Marchesini, H. Padmore, T. Tyliszczak, T. Warwick, X. Shi, J. Lee, Y.-S. Yu, J. Cabana, J. Joseph, H. Krishnan, T. Perciano, F. R. N. C. Maia and D. A. Shapiro, *Appl. Phys. Lett.*, 2017, **110**, 063101.

38 M. Hirose, N. Ishiguro, K. Shimomura, N. Burdet, H. Matsui, M. Tada and Y. Takahashi, *Angew. Chem., Int. Ed.*, 2018, **57**, 1474–1479.

39 M. Hirose, N. Ishiguro, K. Shimomura, D. N. Nguyen, H. Matsui, H. C. Dam, M. Tada and Y. Takahashi, *Commun. Chem.*, 2019, **2**, 1–7.

40 H. Uematsu, N. Ishiguro, M. Abe, S. Takazawa, J. Kang, E. Hosono, N. D. Nguyen, H. C. Dam, M. Okubo and Y. Takahashi, *J. Phys. Chem. Lett.*, 2021, **12**, 5781–5788.

41 M. Abe, F. Kaneko, N. Ishiguro, T. Kubo, F. Chujo, Y. Tamenori, H. Kishimoto and Y. Takahashi, *J. Phys. Chem. C*, 2022, **126**, 14047–14057.

42 S. G. Urquhart, X-ray Spectroptychography, *ACS Omega*, 2022, **7**, 11521–11529.

43 B. M. Weckhuysen, *Angew. Chem., Int. Ed.*, 2009, **48**, 4910–4943.

44 T. Hatsui, M. Omodani, T. Kudo, K. Kobayashi, T. Imamura, T. Ohmoto, A. Iwata, S. Ono, Y. Kirihara, T. Kameshima, H. Kasai, N. Miura, N. Kuriyama, M. Okihara, Y. Nagatomo, M. Nagasaki, T. Watanabe and M. Yabashi, Proceedings of the 2013 International Image Sensor Workshop (IISW), Snowbird, Utah, USA, June, 2013, Article No. 3.05.